Consistency of Planck, ACT, and SPT constraints on magnetically assisted recombination and forecasts for future experiments

Silvia Galli,[1,*] Levon Pogosian,[2,†] Karsten Jedamzik,[3,‡] and Lennart Balkenhol[4,§]

[1]*Institut d'Astrophysique de Paris, UMR 7095, CNRS & Sorbonne Université, 98 bis boulevard Arago, 75014 Paris, France*
[2]*Department of Physics, Simon Fraser University, Burnaby, BC, V5A 1S6, Canada*
[3]*Laboratoire de Univers et Particules de Montpellier, UMR5299-CNRS, Universite de Montpellier, 34095 Montpellier, France*
[4]*School of Physics, University of Melbourne, Parkville, VIC 3010, Australia*

(Received 15 September 2021; accepted 17 December 2021; published 11 January 2022)

Primordial magnetic fields can change the recombination history of the Universe by inducing clumping in the baryon density at small scales. They were recently proposed as a candidate model to relieve the Hubble tension. We investigate the consistency of the constraints on a clumping factor parameter b in a simplistic model, using the latest CMB data from Planck, ACT DR4 and SPT-3G 2018. For the combined CMB data alone, we find no evidence for clumping being different from zero, though when adding a prior on H_0 based on the latest distance-ladder analysis of the SH0ES team, we report a weak detection of b. Our analysis of simulated datasets shows that ACT DR4 has more constraining power with respect to SPT-3G 2018 due to the degeneracy breaking power of the temperature (TT) band powers (not included in SPT). Simulations also suggest that the temperature cross polarisation (TE) and the polarisation (EE) power spectra of the two datasets should have the same constraining power. However, the ACT DR4 TE,EE constraint is tighter than expectations, while the SPT-3G 2018 one is looser. While this is compatible with statistical fluctuations, we explore systematic effects which may account for such deviations. Overall, the ACT results are only marginally consistent with Planck or SPT-3G, at the 2–3σ level within ΛCDM $+ b$ and ΛCDM, while Planck and SPT-3G are in good agreement. Combining the CMB data together with BAO and SNIa provides an upper limit of $b < 0.4$ at 95% c.l. ($b < 0.5$ without ACT). Adding a SH0ES-based prior on the Hubble constant gives $b = 0.31^{+0.11}_{-0.15}$ and $H_0 = 69.28 \pm 0.56$ km/s/Mpc ($b = 0.41^{+0.14}_{-018}$ and $H_0 = 69.70 \pm 0.63$ km/s/Mpc without ACT). Finally, we forecast constraints on b for the full SPT-3G survey, Simons Observatory, and CMB-S4, finding improvements by factors of 1.5 (2.7 with Planck), 5.9 and 7.8, respectively, over Planck alone.

DOI: 10.1103/PhysRevD.105.023513

I. INTRODUCTION

Magnetic fields are ubiquitous in galaxies and clusters of galaxies, and there are good reasons to suspect that the Universe is magnetized on cosmological scales (see [1–3] for reviews). Cosmic magnetism may well be of astrophysical origin, having been generated over the course of the structure formation, but the full story of how this would happen is far from complete. Alternatively, all of the observed fields would be simply explained if a primordial magnetic field (PMF) of a certain strength was already present in the plasma prior to the onset of gravitational collapse. Such fields could have been generated in cosmic phase transitions [4] or during inflation [5,6] and, if detected, would provide an exciting new window into the early Universe. With astrophysical mechanisms being difficult to rule out, only cosmic microwave background (CMB) observations could unambiguously prove the primordial origin of the observed fields.

A PMF present in the plasma before and during recombination would leave a variety of imprints in the CMB [7–58,58–63]. In particular, as first pointed out in [52] and later confirmed by detailed magnetohydrodynamics (MHD) simulations [64], the PMF induces baryon inhomogeneities (clumping) on scales below the photon mean free path, enhancing the process of recombination and making it complete at an earlier time. This lowers the sound horizon at last scattering $r_\star$ that sets the locations of the acoustic peaks in the CMB anisotropy spectra, measured with an exquisite precision by Planck [65] and other experiments [e.g., [66–68]]. Consequently, this mechanism provides the tightest bounds on the PMF from the CMB,

*gallis@iap.fr
†levon@sfu.ca
‡karsten.jedamzik@umontpellier.fr
§lbalkenhol@student.unimelb.edu.au

capable of probing fields of ∼0.01–0.05 nano-Gauss (nG) post-recombination strength [64], well below the ∼nG upper bounds based on other CMB signatures [58]. As one is entering uncharted terrain in terms of the field strength, there is an actual possibility of detecting the PMF. In fact, the magnetically assisted recombination was recently shown [69] to be a promising way of alleviating the Hubble tension, discussed further below. This requires a comoving pre-recombination field strength of ∼0.05 nG, which happens to be of the right order to naturally explain all the observed galactic, cluster and extragalactic fields.

The Hubble tension refers to the discrepancy between the value of the Hubble constant H_0 determined by fitting the ΛCDM model to CMB data and H_0 determined directly from the slope of the Hubble diagram. The statistical significance of the tension is primarily driven by the difference between the measurement of $H_0 = 73.2 \pm 1.3\ \mathrm{km/s/Mpc}$ [70] (and more recently [71]) using Cepheid calibrated supernova and the Planck best-fit ΛCDM value of $H_0 = 67.36 \pm 0.54\ \mathrm{km/s/Mpc}$ [72]. Other independent measurements tend to reenforce the tension, with a general trend that all measurements that do not rely on a model of recombination give H_0 in the 69–73 km/s/Mpc range [73–78], while estimates based on the standard treatment of recombination are robustly around 67–68 km/s/Mpc [79–82]. This might point to a missing ingredient in the model of recombination. As lowering $r_\star$ is what one needs to bring the two groups of measurements closer, the magnetically induced baryon clumping could turn out to be that missing piece of the puzzle.

Adding baryon clumping to the ΛCDM model creates an approximate degeneracy between the clumping amplitude parameter b and the inferred Hubble constant. Whereas the Planck data by itself prefers zero clumping, the inclusion of the local H_0 measurements as a prior result in a 3–4σ detection of b, while still providing a good fit to Planck and with other cosmological parameters hardly changed from that of the best-fit ΛCDM model. Reducing $r_\star$, while being a prerequisite for resolving the H_0 discrepancy, is not necessarily sufficient by itself, as there is much more information in the CMB temperature and polarization spectra than the locations of the acoustic peaks [83]. In particular, the Silk damping and the overall amplitude of polarization are sensitive to modifications of recombination history, along with the balance of power between the small and large scale polarization anisotropies [84]. In this light, it is perhaps remarkable that baryon clumping provides an acceptable fit to the Planck data with $H_0 \sim 70\ \mathrm{km/s/Mpc}$ [69]. In fact, it is not the worsening of the CMB fit, but preserving the agreement with the baryon acoustic oscillations (BAO) data that prevents achieving an even higher value of H_0 in this model, which is a general problem for all solutions of the H_0 tension based on lowering $r_\star$ [85] (although more extended models might elude these constraints, see e.g., [86]). As a byproduct, baryon clumping also slightly relieves the σ_8 tension, a ∼2–3σ difference between the values of matter fluctuation amplitude and matter density inferred from weak lensing surveys and CMB constraints within the ΛCDM model [87,88].

The aim of this paper is to examine the impact of baryon clumping on CMB polarization, focusing on the potentially distinguishing signatures on small angular scales. The small scale temperature and polarization anisotropy spectra were recently measured from the Atacama Cosmology Telescope fourth data release (ACT DR4) [68] and the South Pole Telescope Third Generation (SPT-3G) 2018 data [67], and are expected to become more accurate after the release of the Advanced ACTpol [89] and SPT-3G full survey [90] data and with future data from the Simons Observatory (SO) [91] and CMB-Stage 4 (CMB-S4) [92]. Very recently, [93] have performed a similar study, using, however, only the combination of Planck and ACT DR4 data. They conclude that the addition of ACT DR4 strengthens the constraints on clumping compared to Planck alone. Another very recent study [94] used the Planck data to constrain small-scale isocurvature baryon perturbations, with the conclusion that they cannot alleviate the Hubble tension. Their results, however, are based on linear perturbation theory and do not apply to the nonlinear baryon clumping induced by PMFs. Furthermore, even mildly nonlinear isocurvature fluctuations would be strongly constrained by the Big Bang Nucleosynthesis (BBN) [95]. To the best of our knowledge, there are no other scenarios leading to nonlinear, space-filling density fluctuations before recombination without violating the BBN constraints [69]. While this paper was in its final editing stages, [96] also reported constraints on clumping from Planck and forecasts for future experiments, using, however, a model with more degrees of freedom compared to ours and not including the ACT DR4 and SPT-3G 2018 data. Here, instead, we calculate and examine in detail the constraints from the latest ACT and SPT datasets, alone and in combination with Planck. We test their consistency and robustness against systematic effects, and combine them with other datasets such as the eBOSS DR16 BAO compilation from [82] and the Pantheon supernovae (SN) sample [97]. To sample the posterior distributions of cosmological datasets we use the CosmoMC code [98], while we calculate the evolution of the recombination history through RECFAST [99].

The rest of the paper is organized as follows. Section II briefly reviews the physics of baryon clumping induced by PMFs and its impact on recombination and CMB polarization signatures that can help distinguish between ΛCDM and ΛCDM$+b$. In Sec. III we derive constraints on the ΛCDM$+b$ model from Planck, ACT DR4 and SPT-3G 2018, and examine the consistency between them investigating the impact of possible systematic effects. In Sec. IV we provide joint constraints from CMB, BAO, and SN data. Forecasts of constraints on clumping from SPT-3G, SO and CMB-S4 are given in Sec. V. We conclude with a discussion in Sec. VI.

II. RECOMBINATION WITH MAGNETIC FIELDS AND THE IMPACT ON THE CMB ANISOTROPIES

We start this section with a review of the physical mechanism behind the magnetically sourced baryon clumping, and the subsequent effect on recombination and the CMB anisotropies.

A. Recombination with primordial magnetic fields

A PMF can be generated either during cosmic phase transitions or during inflation. The resultant field is stochastic, but statistically homogeneous and isotropic. The PMF generated in phase transitions would have a very blue spectrum, whereas the simplest inflationary magnetogenesis models predict a scale-invariant PMF. For details on their evolution well before recombination we refer the reader to [100].

PMFs generate baryonic density fluctuations on small scales before recombination. These scales, e.g., ~ 1 kpc for a field of ~ 0.1 nG,[1] are well below the photon mean free path, $l_\gamma \sim 1$ Mpc. The electron-baryon fluid is initially at rest and uniform. The magnetic stress term in the Euler equation, $\propto \vec{B} \times (\nabla \times \vec{B})$, induces fluid motions in the plasma, which, via the continuity equation, lead to density fluctuations. The amplitude of the density fluctuations is limited by the backreaction of the fluid due to pressure gradients. A simple analytic estimate made in [52] showed that the amplitude of baryonic density fluctuations follows

$$\frac{\delta\rho_b}{\rho_b} \simeq \min\left[1, \left(\frac{c_A}{c_b}\right)^2\right], \qquad (1)$$

where $c_A = B/\sqrt{4\pi\rho_b}$ is the Alfven speed, with B being the magnetic field strength, and c_b is the baryonic speed of sound, excluding contributions from photons as they are free-streaming on small scales. Since, at recombination, $c_A = 4.34\ \mathrm{km/s}(B/0.03\ \mathrm{nG})$ and $c_b = 6.33$ km/s, even fairly weak fields may generate order unity density fluctuations on small scales. This simple estimate has subsequently been confirmed by full numerical simulations [64].

It is important to note that density fluctuations can not exceed unity by much, as the source of the density fluctuations, the PMF, dissipates at some point. Along with the PMF, the produced density fluctuations dissipate as well. But, since all PMFs are described by a continuous spectrum, when the PMF and density fluctuations dissipate on a particular scale, density fluctuations are generated on a somewhat larger scale, where the PMF has not had enough time to dissipate. It is thus unavoidable to have a clumpy baryon fluid shorty before recombination, if a PMF is present. The amplitude of the clumpiness is unknown, as it is determined by the unknown PMF strength. Since the phase transition generated PMFs have a blue spectrum, with most of the power concentrated near the dissipation scale, they shed a significant fraction of their power with each e-fold of expansion, as the peak of the spectrum moves to larger scales. Consequently, they produce larger density fluctuations some time before recombination than immediately before recombination. This is not the case for the scale-invariant PMF.

The magnetically induced inhomogeneities are on scales much too small (i.e., $\ell \sim 10^6$–10^7) to be observed directly in the CMB spectrum. However, the baryon clumping has an indirect effect on the CMB anisotropies. As the recombination rate is proportional to the square of the electron density n_e, and since, generally, the spatial average $\langle n_e^2 \rangle > \langle n_e \rangle^2$ in a clumpy Universe, the recombination rate is enhanced compared to that in ΛCDM, so that recombination occurs earlier. This, in turn, reduces the sound horizon $r_\star$ at last scattering, the ingredient that many propositions to solve the Hubble tension employ. There is a further, more subtle, effect of the PMF generated baryon clumping on recombination. Local peculiar velocity gradients induced by the PMF influence the local Lyman-α escape rate, with expanding (contracting) regions having a higher (lower) Lyman-α escape rate due to redshifting (blueshifting) [94,101,102].

The evolution of the cosmic electron density depends on the full shape of the baryon density probability distribution function (PDF), and not only on its second moment, referred to as the clumping factor

$$b \equiv \left(\frac{\langle \rho_b^2 \rangle - \langle \rho_b \rangle^2}{\langle \rho_b \rangle^2}\right). \qquad (2)$$

The shape of the baryon density PDF is currently unknown, and neither is its evolution before recombination. Furthermore, the statistics of peculiar flows is not known. In the absence of detailed compressible numerical MHD simulations, which would reveal the PDF and peculiar velocity statistics, Refs [52,69] proposed a simple three-zone toy model to estimate the effects of clumping on the CMB anisotropies. This model computes the average ionization fraction over three different regions occupying volume fractions f_V^i and having densities $\rho_b^i = \langle \rho_b \rangle \Delta_i$, where $\langle \rho_b \rangle$ is the average baryon density. Here, somewhat arbitrarily for the model M1, the values $\Delta_1 = 0.1$, $f_V^2 = 1/3$, and $\Delta_2 = 1$ are chosen, with the remaining parameters determined by the constraint equations

$$\sum_{i=1}^{3} f_V^i = 1, \quad \sum_{i=1}^{3} f_V^i \Delta_i = 1, \quad \sum_{i=1}^{3} f_V^i \Delta_i^2 = 1 + b. \qquad (3)$$

Modifications to the Lyman-α escape rate are neglected. We will follow this method here, but *alert* the reader to the fact that details of the PDF and its evolution, as well as a modified Lyman-α escape rate, could have an impact on our conclusions regarding the effects of PMF on the CMB.

[1] All cited length scales and field strengths are comoving.

The current paper rather constrains static baryon clumping as a toy model.

B. The impact on CMB anisotropies

As discussed previously, baryon clumping facilitates recombination, shifting the peak of the visibility function to an earlier epoch. Along with a smaller $r_\star$, this means that CMB polarization is produced earlier, at a somewhat higher value of the speed of sound c_S. As the amplitude of polarization is set by the temperature quadrupole, which is derived from the dipole, which in turn is set by the time derivative of the monopole being proportional to c_S [84], one generally expects to have a higher polarization amplitude with clumping. More importantly, clumping has a broadening effect on the visibility function, due to overdense baryon pockets recombining earlier and underdense baryon pockets recombining later. The broadening also tends to enhance polarization, because of the longer period of time during which polarization can be generated.

These effects can be seen in Fig. 1, which compares the visibility functions[2] in the ΛCDM model, an unrealistic model in which $b = 2$ with all other parameters kept the same, and the $\Lambda\mathrm{CDM} + b$ model that best fits the combination of Planck and the SH0ES prior on H_0. The broadening effect is apparent from the lower peak, since the plotted visibility function is normalized to integrate to unity. This is in contrast to the implicit statement in [93] that the visibility function is narrower in clumping models.

We note that, while the general trends in the visibility function are common to all clumping models, the quantitative details are dependent on the shape and the evolution of the baryon density PDF. The visibility functions shown in Fig. 1 correspond to the particular case of the M1 model, first introduced in [52]. A second PDF guess, M2, was considered in [69], to demonstrate the model dependence of the results. Because M1 is the more promising of the two for relieving the Hubble tension, all our quantitative results are based on M1.

Another change compared to ΛCDM is a modification of the Silk damping scale r_D. There are three competing effects: r_D decreases due to an earlier recombination, increases due to a smaller electron density before recombination caused by an earlier broad helium recombination, and increases due to the broadening of the visibility function. Note that much of the Silk damping actually occurs right at recombination, where the visibility function is of order unity, such that details of the visibility function matter. The first effect, by itself, would reduce the Silk damping, pushing the onset of the damping tail to higher ℓ.

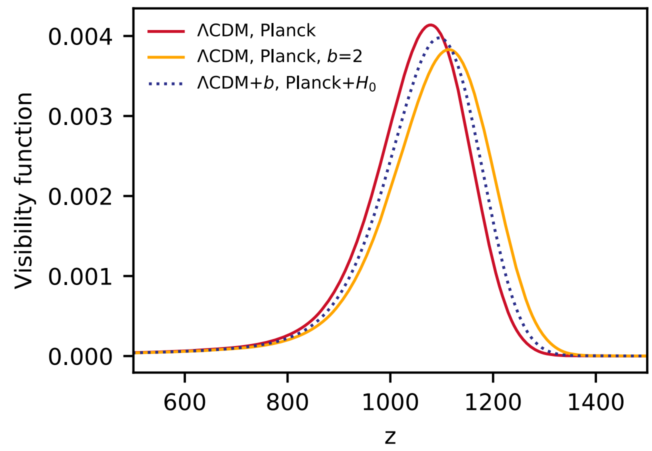

FIG. 1. Impact of baryon clumping on the CMB visibility function in units of redshift. We show the Planck ΛCDM best-fit (solid red line), the case where all cosmological parameters are set to the best-fit ΛCDM and the amplitude of clumping is set to $b = 2$ (solid orange line), and the $\Lambda\mathrm{CDM} + b$ Planck + SH0ES best-fit model (dotted blue line). Clumping shifts the peak of the visibility function to earlier times, and increases its width.

The second and third effects, however, are also important and are opposite to the first. The balance between them is model-dependent and varies with the clumping factor. In M1, with parameters that fit the data, there is less Silk damping. But in the best-fit M2 model, the Silk damping is

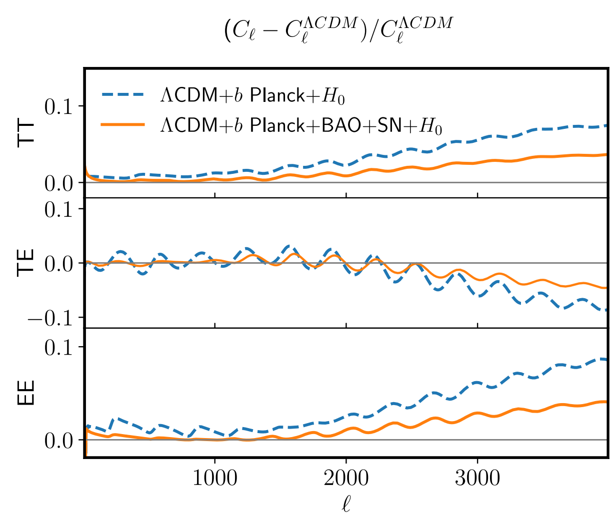

FIG. 2. Impact of baryon clumping on CMB power spectra. The relative difference between the Planck best-fit ΛCDM and the M1 model best-fit to Planck + SH0ES (blue dashed line) and Planck + BAO + SN + SH0ES (orange solid line). In the case of TE, to avoid divisions by zero, we compute $(C_\ell - C_\ell^{\Lambda\mathrm{CDM}})/C_\ell^{\mathrm{ref}}$, where C_ℓ^{ref} is the absolute value of $C_\ell^{\Lambda\mathrm{CDM}}$ convolved with a Gaussian of width $\sigma_\ell = 100$ centred at ℓ. Baryon clumping leaves signatures in the small-scale anisotropies of the temperature and polarization spectra.

[2] The visibility function in Fig. 1, $g(z)$, is the probability density distribution with respect to redshift, i.e., $dP = g(z)dz$. We checked that we obtain a similar impact of baryon clumping on the visibility function when it is defined with respect to conformal time η instead of z, $g(\eta) = g(z)dz/d\eta$.

virtually identical to that in the best-fit ΛCDM. In M1, at (observationally disallowed) high values of b, the Silk damping is actually enhanced (see also [96] for the evolution of the damping scale as a function of b in a different PMF model from the one used here). It should be noted that clumping evolution, which is unknown at present, is yet another source of uncertainty. If clumping was stronger at $z \sim 3000$, then helium recombination could be the dominant effect, inducing more Silk damping.

Figure 2 compares the CMB spectra in the Planck best-fit ΛCDM to those in the M1 model that best fits the combinations of Planck + SH0ES and Planck + BAO + SN + SH0ES. We see that the temperature (TT), polarisation (EE), and temperature cross polarisation (TE) power spectra are enhanced at high ℓ due to reduced Silk damping (this happens in a region of multipoles where TE is mostly negative, i.e., there is an anticorrelation between T and E, hence, for TE, the enhancement translates into a more negative signal). At $\ell \lesssim 20$, the polarization is reduced, which is due to the lower best fit value of the optical depth τ. This indicates that high resolution CMB measurements could be a key discriminant in constraining the magnetically sourced recombination.

III. CONSTRAINING CLUMPING WITH PLANCK, ACT AND SPT-3G

As discussed earlier, high resolution CMB temperature and polarization measurements play an important role in constraining the baryon clumping. Hence, it is interesting to investigate the implications of the new data from the ACT and SPT collaborations for this scenario. In what follows, we compare and examine the constraints on clumping from Planck, ACT DR4 and SPT-3G 2018, in some detail, including performing tests on simulated data, with the aim of revealing the underlying causes of any differences between them. The datasets we consider are:

(i) Planck: we use the 2018 final release of the Planck data [65]. At large angular scales, in temperature we use the TT Commander likelihood ($\ell = 2$–29), while in polarization we use SimAll ($\ell = 2$–29, EE only). For high multipoles, we use the Plik likelihood in TT ($\ell = 30$–2508), TE and EE ($\ell = 30$–1997 in EE and TE). Finally, we use the Planck lensing reconstruction likelihood;

(ii) SPT-3G 2018: we use the first release of the SPT-3G data described in [67]. This features EE and TE band powers at $\ell = 300$–3000, obtained from observations of 1500 deg^2 taken over four months in 2018 (half of a typical observing season) at three frequency bands centered on 95, 150, and 220 GHz. Only about half of the detectors were operable during these observations;

(iii) ACT DR4: we use the fourth release of the ACT data as included in the frequency-combined, CMB-only ACTPollite likelihood [68,81], in TT TE EE. These are based on ACTpol observations taken in 2013–2016 of 6000 deg^2 of the sky at 98 and 150 Ghz, as well as the ACT DR2 observations in intensity described in [103];

When using the ACT DR4 and SPT-3G 2018 likelihoods alone, we use a Gaussian prior on the optical depth to reionization of $\tau = 0.0543 \pm 0.0073$, following [72]. When sampling the $\Lambda\mathrm{CDM} + b$ model, we set a uniform prior on clumping with $0 \leq b \leq 2$. Note that since b is weakly constrained in many of the cases considered in the following, a different choice of priors (e.g., a log-uniform one) could have an impact on results. However, we reckon that this choice would not change the qualitative conclusions of this paper.

A. Separate Planck, ACT and SPT constraints

Figures 3 and 4 compare the constraints on the $\Lambda\mathrm{CDM} + b$ model obtained separately from Planck, ACT DR4 and SPT-3G 2018, also reported in Table I. We highlight three results from these comparisons. First, one can see that the ACT DR4 constraint on b is much stronger compared to the one from SPT-3G 2018. This is interesting, since for other models, such as ΛCDM and its extensions considered in [81,104], the constraints from the two experiments are comparable.[3] Second, ACT DR4 prefers low values of ω_{b} and high values of n_{s}, as already pointed out for the ΛCDM model in [81]. Third, SPT-3G 2018 prefers values of b different from zero, albeit with a low statistical significance (less than 2σ). In what follows, we explore in depth the source of these differences.

B. ACT

We first investigate the difference in constraining power between ACT DR4 and SPT-3G 2018. The ACT DR4 likelihood includes temperature and polarization TT,TE,EE spectra up to multipoles of $\ell_{\max} = 4000$. On the contrary, the SPT-3G 2018 likelihood includes information from only TE,EE at multipoles up to $\ell_{\max} = 3000$.[4]

To assess the expected difference in constraining power, we produce synthetic band powers for ACT DR4 and SPT-3G 2018 using the SPT-3G 2018 ΛCDM best-fit as a

[3]For example, within ΛCDM, the ACT constraints are stronger than SPT's only for n_{s} and $\ln(10^{10}A_{\mathrm{s}})$, by 30%. We find this is due to the fact that ACT also includes the TT data, while SPT does not.

[4]Note that comparing band power error bars to investigate the constraining power of the two experiments can lead to wrong conclusions. The band powers are correlated—mostly positively correlated in case of ACT, while the SPT band powers feature strong anti-correlations in adjacent bins. Furthermore, the ACT-Pollite power spectrum error bars include uncertainties from nuisance parameters, while those of SPT do not, since those parameters are marginalized over at the parameter estimation level.

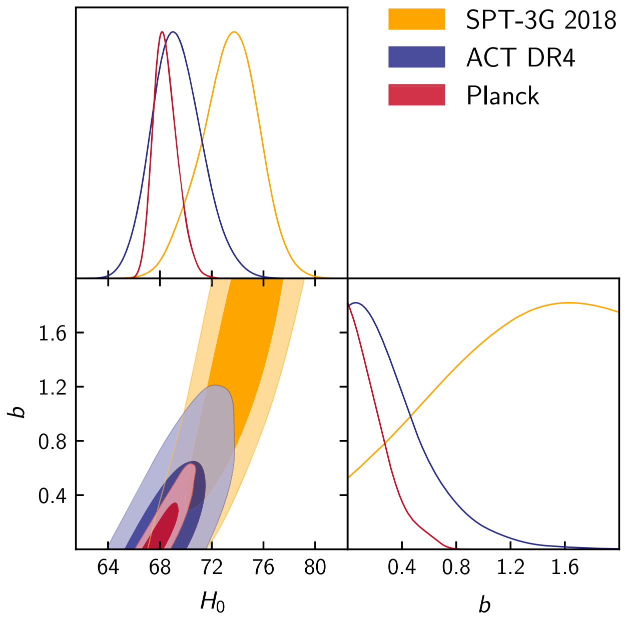

FIG. 3. Two-dimensional posterior distributions of the clumping factor b and H_0 in the ΛCDM + b model for SPT-3G 2018 (yellow), ACT DR4 (blue), and Planck (red). From Planck and ACT DR4 we infer best-fit values consistent with no clumping, whereas the posterior for the SPT-3G 2018 data peaks at b larger than one, albeit with low statistical significance.

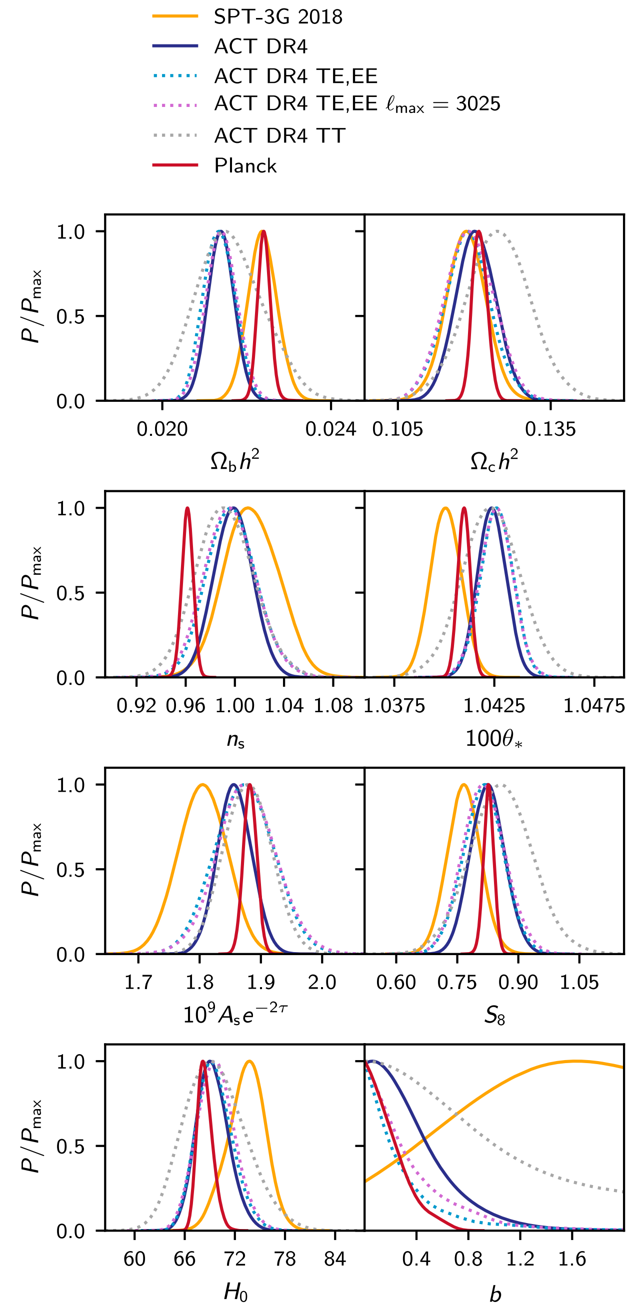

FIG. 4. One-dimensional posterior distributions of cosmological parameters in the ΛCDM + b model. We show results for SPT-3G 2018 (yellow), ACT DR4 (blue), and Planck (red). We also show the impact of separately fitting ACT DR4 TE,EE (dotted cyan) and ACT DR4 TT (dotted gray).

fiducial model.[5] The simulated band powers are then analyzed using the same likelihood and nuisance parameters as for the real data. The constraints on b from such simulated datasets are shown in Fig. 5.

From these simulations, we see that the constraining power of the ACT DR4 and SPT-3G 2018 TE,EE spectra is practically equal.[6] It is the addition of intensity information in the full ACT data that helps to break degeneracies between n_s, $A_s e^{-2\tau}$, and other parameters, which in turn leads to a tighter constraint on b, as seen in Fig. 6.

However, the effect of removing TT from the real ACT data is opposite to what is expected from simulations. In particular, the ACT TE,EE constraint is *stronger* than that from the full ACT likelihood with TT,TE,EE, as shown in Fig. 4. We verified that cutting the ACT multipoles at $\ell > \ell_{\max} \sim 3000$, as done for SPT-3G 2018, has a negligible impact on the constraints.

As discussed in [81], there are inconsistencies between the ACT and Planck results which might be solved by a recalibration of the ACT TE spectra by ~5%. While such a recalibration is not justified by any known source of systematics, we test how this would impact our results. We thus modified the ACT likelihood in order to multiply the TE theory spectra (both for the deep and the wide survey) by a factor $y_p^{TE} = 1.05$, while maintaining the

[5]The actpollite dr4 likelihood only has only one nuisance parameter, the y_p polarization calibration which multiplies the theory spectra as, i.e., $C_\ell^{TE} = y_p C_\ell^{th,TE}$, $C_\ell^{EE} = y_p^2 C_\ell^{th,EE}$. In the fiducial model for the synthetic band powers, we set $y_p = 1$. On the other hand, the SPT-3G 2018 likelihood has several nuisance parameters, which we set to the best-fit values of the ΛCDM model in the simulations.

[6]We modified the actpollite dr4 likelihood in order to use the combination of TE,EE without TT. When using TE,EE from ACT, we set a Gaussian prior of $y_p = 1 \pm 0.01$, in line with the $\mathcal{O}(1\%)$ calibration prior in the SPT likelihood.

TABLE I. Constraints on the clumping b (at 95% c.l.) and on H_0 (at 68% c.l.) from current CMB data. We note that our adopted prior of $b < 2$ significantly impacts the SPT-3G 2018 constraints on b and H_0. Without this prior, SPT-3G 2018 would allow much higher values.

	Planck	SPT-3G 2018	ACT DR4	Planck +SPT-3G 2018	Planck +ACT DR4
b	<0.51	<2	<1.2	<0.54	<0.31
H_0	$68.5^{+0.74}_{-1.1}$	$73.4^{+2.4}_{-2.0}$	$69.3^{+1.7}_{-2.1}$	$68.7^{+0.76}_{-1.0}$	$68.1^{+0.63}_{-0.74}$

TABLE II. Consistency between Planck, ACT and SPT. We evaluate the PTE for the ΛCDM or $\Lambda\mathrm{CDM}+b$ models including ω_b, ω_c, θ^*, n_s, $A_s e^{-2\tau}$ (and b), and report in parenthesis the deviation in units of Gaussian σ.

	ΛCDM	$\Lambda\mathrm{CDM}+b$
Planck, SPT-3G 2018	$12\% + (1.2\sigma)$	$6\% + (1.8\sigma)$
Planck, ACT DR4	$0.5\% + (2.7\sigma)$	$1.5\% + (2.4\sigma)$
SPT-3G 2018, ACT DR4	$0.5\% + (2.7\sigma)$	$0.8\% + (2.6\sigma)$

baseline y_p polarization calibration parameter for the EE spectra with a Gaussian prior of $y_p = 1 \pm 0.005$. We find that, indeed, such a recalibration can weaken the constraint on b from ACT TE,EE by about 30%, from $b < 1.0$ (ACT TE,EE) to $b < 1.3$ (ACT TE,EE, $y_p^{TE} = 1.05$) at 95% c.l., as shown in Fig. 7. However, the constraint is still stronger than the one expected from simulations by about a factor

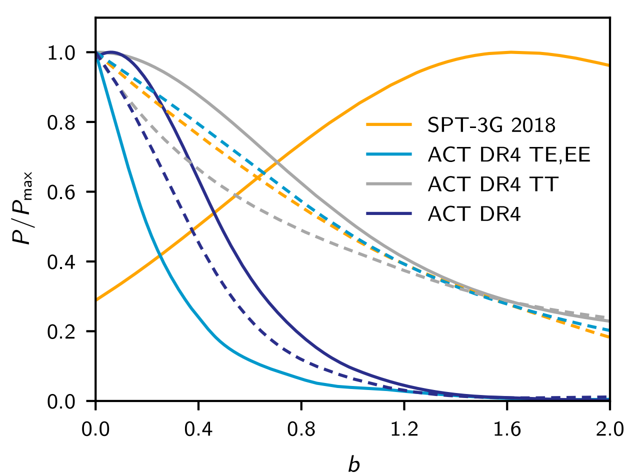

FIG. 5. Constraints on b from simulated (dashed) and real (solid) data for SPT-3G 2018 (yellow) and ACT DR4 (blue). For ACT, we also show the results for TE,EE (cyan) and TT (gray). According to simulations, the tight constraint on b from ACT is due to the combination of TT and TE,EE. Excising the intensity information, SPT-3G 2018 and ACT DR4 should have the same constraining power on b. However, fluctuations in the real data and the physical bound $b > 0$ make the ACT TE,EE data look much more constraining than that from SPT.

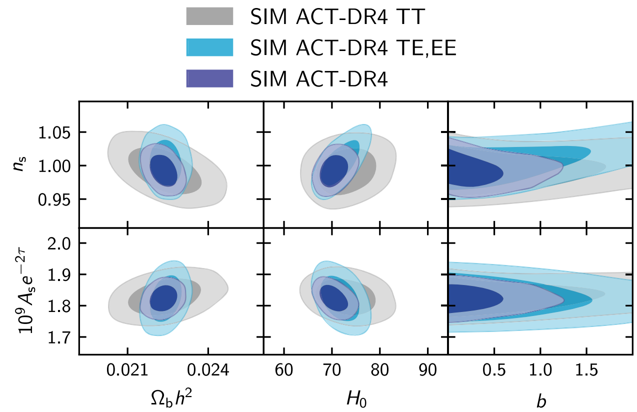

FIG. 6. Two-dimensional posterior distributions for n_s, the amplitude of power spectra $A_s e^{-2\tau}$ and other cosmological parameters for simulated ACT DR4 band powers in the $\Lambda\mathrm{CDM}+b$ model. The simulations assume a ΛCDM fiducial model with $b = 0$. The combination of TT and TE,EE helps to lift degeneracies and to tighten the constraint on b.

of 2, indicating that such a recalibration could only partially account for the difference between the two. On the other hand, the recalibration shifts n_s and ω_b constraints towards better agreement with Planck, similar to the ΛCDM case explored in [81].

Interestingly, the overall ACT TT,TE,EE constraint is in good agreement with expectations, as shown in Fig. 5. Also in this case, we verify the impact of a recalibration of TE. We either place a uniform prior on y_p^{TE}, or set it to $y_p^{TE} = 1.05$. We find that this weakens the 95% c.l. upper limit on clumping by a smaller amount, from $b < 0.96$ (ACT TT,TE,EE) to $b < 1.08$ ($y_p^{TE} = 1.05$) or $b < 1.11$ (free y_p^{TE}), as shown in Fig. 7. Remarkably, the peak of the posterior distribution of H_0 is robust against these changes.

To summarize, the ACT DR4 constraints on b are expected to be stronger than those from SPT-3G 2018 because the ACT TT information helps to break degeneracies between b and other cosmological parameters. Simulations show that ACT TE,EE and SPT TE,EE should have equivalent power to constrain b. However, the constraints based on the real ACT data behave curiously when TT is excised, with the bounds on clumping becoming tighter when only TE,EE are used. While we find that a TE recalibration can impact the b constraints, the ACT TE,EE results remain somewhat stronger than what is expected from simulations. At present it is thus unclear whether this is due to a statistical fluctuation or a systematic effect. Overall, the full ACT TT,TE,EE constraint is in good agreement with expectations.

C. SPT

Next, we investigate the preference by SPT-3G 2018 for high values of b. The difference in the best-fit χ^2 with respect to ΛCDM is only $\Delta_\chi^2 = 1.7$, thus making this

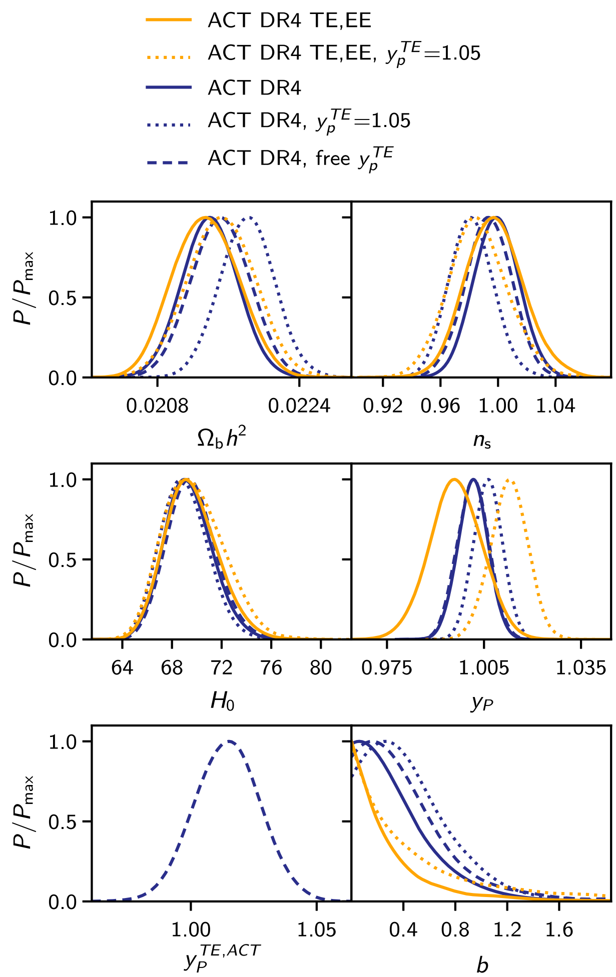

FIG. 7. Impact of a recalibration of the ACT TE power spectra y_p^{TE} on the ACT TT,TE,EE (blue) and ACT TE,EE (yellow) results. We show the reference case $y_p^{TE} = 1$ (solid), the case where we fix $y_p^{TE} = 1.05$ (dashed), and the case where we place a uniform prior on y_p^{TE} (dotted). For the TE,EE cases, we set a prior on the polarization calibration of $y_p = 1.0 \pm 0.01$. For all cases with $y_p^{TE} \neq 1$, we adjust y_p to only affect the EE spectra. A change in the TE calibration weakens the constraints on b and shifts n_s (ω_b) to lower (higher) values, towards the Planck results.

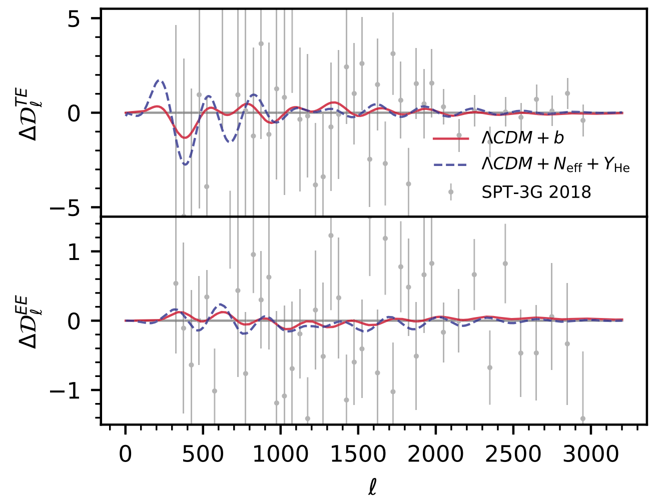

FIG. 8. Difference in best-fit models of the SPT-3G 2018 data with respect to ΛCDM. We show the case of $\Lambda\mathrm{CDM} + b$ (solid red) and $\Lambda\mathrm{CDM} + N_{\mathrm{eff}} + Y_{\mathrm{HE}}$ (dashed blue). The SPT-3G 2018 data residuals with respect to ΛCDM are shown in gray. The $\Lambda\mathrm{CDM} + b$ and $\Lambda\mathrm{CDM} + N_{\mathrm{eff}} + Y_{\mathrm{HE}}$ models both fit similar features in the SPT power spectra.

compatible with a statistical fluctuation. We find that this deviation is possibly sourced by the same features in the power spectra that also cause other deviations from ΛCDM in the SPT results, at a comparable low statistical significance. In particular, [104] reports a high number of relativistic species N_{eff} and low Helium abundance Y_{HE} compared to the ΛCDM expectation, when these are fit simultaneously. We find that the SPT-3G 2018 best-fit power spectra for the $\Lambda\mathrm{CDM} + b$ and $\Lambda\mathrm{CDM} + N_{\mathrm{eff}} + Y_{\mathrm{HE}}$ share key features, as shown in Fig. 8. We cross-checked that for $\Lambda\mathrm{CDM} + b + N_{\mathrm{eff}} + Y_{\mathrm{HE}}$, the deviations with respect to ΛCDM of all three parameters indeed decrease, confirming the connection between the two models. However, we remind the reader that the improvement in $\Delta\chi^2$ for the two models is not statistically significant: $\Delta\chi^2 = 1.7$ and $\Delta\chi^2 = 2$ for one and two additional degrees of freedom for the $\Lambda\mathrm{CDM} + b$ and $\Lambda\mathrm{CDM} + N_{\mathrm{eff}} + Y_{\mathrm{HE}}$ models, respectively.

Furthermore, [104] highlights a slight inconsistency in the mean supersample lensing convergence $\bar{\kappa}$ measured in the SPT-3G sky patch. The expected ΛCDM value for this sky region is $10^3\bar{\kappa}_{\Lambda\mathrm{CDM}} = 0 \pm 0.45$. The SPT-3G 2018 likelihood marginalizes over $\bar{\kappa}$ with a Gaussian prior set by this ΛCDM expectation, in order to break the large degeneracy between $\bar{\kappa}$ and the angular scale of sound horizon θ.

However, the combination of SPT-3G 2018 with Planck, when placing a uniform prior on $\bar{\kappa}$, yields $10^3\bar{\kappa}_{\mathrm{SPT-3G}} = 1.6 \pm 0.56$. We have tested that using this constraint as a prior on $\bar{\kappa}$ instead of $\bar{\kappa}_{\Lambda\mathrm{CDM}}$ does not impact the SPT-3G 2018 results on b.

D. Consistency of Planck, ACT, and SPT

We assess the consistency of the three datasets by comparing their results on cosmological parameters by pairs. In particular, we calculate the parameter χ_p^2 defined as $\chi_p^2 = \Delta_p^T \Sigma^{-1} \Delta_p$, where Δ_p is the difference in the marginalized posterior means obtained by two of the experiments and Σ is the sum of their parameter covariance matrices. We consider the five ΛCDM parameters ω_b, ω_c, θ_*,[7] n_s, $A_s e^{-2\tau}$, together with b. We use the combined amplitude parameter, $A_s e^{-2\tau}$, since the separate A_s and τ constraints are correlated

[7] θ_* is the angular size of the sound horizon at last scattering. This is different from the approximated parameter θ_{MC}, used in COSMOMC to sample the parameter space, and which assumes a ΛCDM recombination model.

across the different experiments due to the common use of a Planck-based prior on τ (see [105,106] for more details). This procedure has a number of limitations, offering only an approximated way of assessing consistency. First, it is only valid for independent experiments. While the SPT-3G 2018 and ACT DR4 observed sky patches do not overlap and are largely independent, and the SPT and Planck correlations can be neglected, there is a correlation between ACT and Planck in TT at $\ell < 1800$ [81]. Furthermore, this procedure assumes that the parameter posterior distributions are Gaussian, so that χ_p^2 can be approximated to have a χ^2 distribution, and this is of course not exactly true for the cases considered. Despite these limitations, we judge that this procedure is good enough to identify major consistency issues between experiments.

Table II reports the probability to exceed (PTE) both for the ΛCDM and the $\Lambda\mathrm{CDM} + b$ models. We judge that datasets with differences larger than 3 Gaussian σ (i.e., the number of standard deviations equivalent to the reported PTE for a Gaussian distribution) are not in sufficient agreement to be combined. While we find a good agreement between SPT and Planck, ACT is consistent with either of the two experiments for both models but with large deviations, at the level of $2-3\sigma$ in all cases. This is in agreement with the findings of [81], who evaluated the consistency of ACT and Planck for the ΛCDM model at the 2.7σ level. We conclude that Planck, ACT DR4 and SPT-3G 2018 are consistent enough to combine them together, although the ACT results are more than 2σ away from the other two experiments.

E. Joint Planck, ACT and SPT constraints

Figure 9 and Table I show the constraints on b when the Planck data are combined with ACT DR4 or SPT-3G 2018. For ACT, we also show constraints from TE,EE and TT separately combined with Planck. We find trends similar to the ones found in Sec. III B. In particular, the combination of Planck + ACT provides a constraint on clumping, $b < 0.31$ at 95% c.l., which is tighter than the one from Planck + SPT: $b < 0.54$ at 95% c.l.[8]

Excising the ACT TT information makes the constraint from Planck + ACT TE,EE stronger, as already found for the case without Planck. This is in contrast with the results of simulations (already described in Sec. III B),[9] which suggest that Planck + ACT TE,EE and Planck + SPT should provide the same constraint $b \lesssim 0.40$ at 95% c.l., as shown in Fig. 9. Finally, we find that the combination of Planck + ACT TT fluctuates to values of b higher than zero by $\lesssim 2\sigma$, while from simulations we expect approximately the same constraining power as for TE,EE.

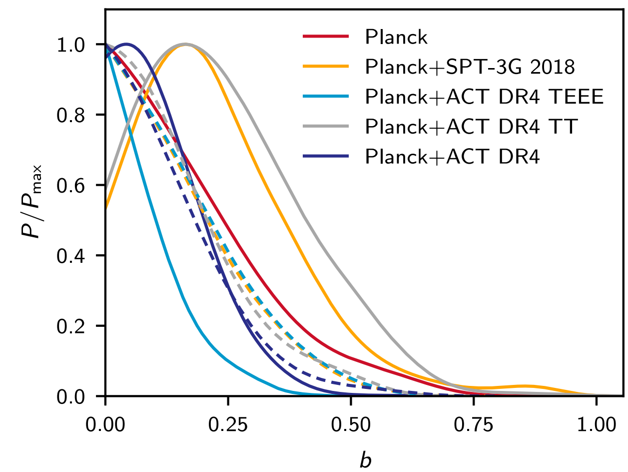

FIG. 9. Constraints on b from the combination of Planck (red) with ACT DR4 (blue) or SPT-3G 2018 (yellow). We also show the cases for Planck + ACT TE,EE (light blue) and Planck + ACT TT (gray). The solid lines represent results from the real data, while the dashed ones are expectations from simulated band powers assuming the ΛCDM model.

We find that the slight preference by SPT for b larger than zero presented in Sec. III C also manifests in the combination with Planck, albeit with very low statistical significance (less than one sigma), providing a constraint of $b < 0.54$ at 95% c.l. Finally, the Planck + ACT results are

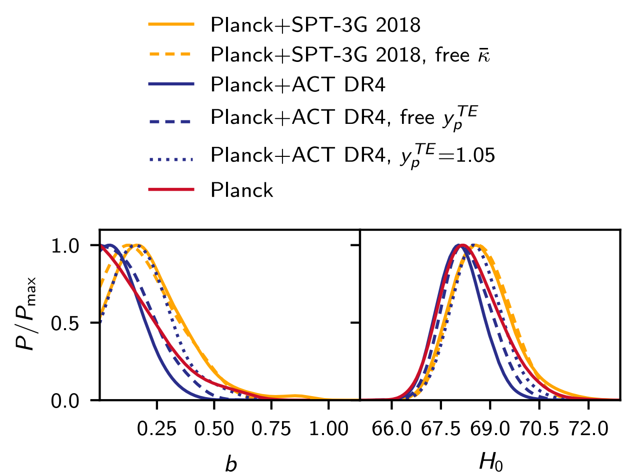

FIG. 10. Impact of systematics on the constraints on b from the combination of Planck with SPT (yellow) or ACT (blue). Placing a uniform prior on the mean lensing convergence for the SPT data (dashed yellow) has a small impact with respect to the reference case (solid). On the contrary, changing the y_p^{TE} calibration of the ACT TE spectra to $y_p^{TE} = 1.05$ (dotted) or placing a uniform prior on it (dashed) weakens the constraints.

[8] We note that our constraint for Planck + ACT is slightly more stringent that the one reported by [93] for the same data combination, $b < 0.42$. This might be due to small differences in the implementation of the M1 model, or by the use of different recombination codes, HyRec [107] in [93], RECFAST [99] in ours.

[9] When simulating the combination of Planck plus ACT or SPT, we use the ΛCDM Planck best-fit as a fiducial model for the ACT and SPT simulated band powers, while we use the real data for Planck.

consistent with expectations and yield $b < 0.31$ ($b < 0.39$ 95% c.l. from simulations).

Similarly to Sec. III B, we verify the impact of possible systematics on the constraints, shown in Fig. 10. A 5% change in the ACT y_p^{TE} calibration weakens the Planck + ACT constraint by ∼50%, to $b < 0.45$ at 95% c.l., producing a smaller than 2σ preference for $b > 0$. Placing a uniform prior on y_p^{TE} has a less dramatic effect, leading to $b < 0.38$ at 95% c.l. and $y_p^{TE} = 1.029 \pm 0.014$, i.e., a 2σ preference for a recalibration in TE. We note that in ΛCDM we find a similar value, $y_p^{TE} = 1.025 \pm 0.014$, rather pointing to a ∼3% recalibration preferred by the data instead of the 5% suggested by [81].

Finally, for Planck + SPT we find that placing a uniform prior on the mean lensing convergence, $\bar{\kappa}$, across the SPT-3G footprint slightly shifts the peak of the b posterior towards zero, though the upper limit does not change appreciably ($b < 0.48$ at 95% confidence). There is no significant change in the H_0 constraint.

IV. THE OBSERVATIONAL STATUS OF THE CLUMPING MODEL

Next, we combine the CMB data with the latest BAO, SN and distance ladder measurements, to derive the most up to date constraints on the ΛCDM + b model. Specifically, we use the eBOSS DR16 BAO compilation from [82] that includes measurements at multiple redshifts from the samples of Luminous Red Galaxies, Emission Line Galaxies, clustering quasars, and the Lyman-α forest [108–111], along with the 6dF [112] and the SDSS DR7 MGS [113] data.[10] We find that the new DR16 BAO data does not make a notable difference compared to the earlier DR12 release when it comes to constraining clumping. For luminosity distances, we use the Pantheon supernovae sample [97]. We also examine constraints with and without the distance ladder estimate of the Hubble constant by the SH0ES team [70], implemented as a gaussian prior of $H_0 = 73.2 \pm 1.3$ km/s/Mpc. We have explicitly checked that using the SH0ES prior on the absolute SN magnitude, as opposed to a gaussian prior on H_0, makes no difference for the models we studied. Also, unlike the analysis in [69], the SH0ES prior in this work is not combined with the determinations of H_0 by the Megamaser Cosmology Project [73] and H0LiCOW [74].

The left panel of Fig. 11 shows the marginalized posteriors for the clumping factor b and H_0 from Planck, Planck + BAO + SN, Planck + SPT + BAO + SN and Planck + ACT + BAO + SN. We see that Planck by itself shows no preference for clumping, with a small increase in the best-fit H_0. Combining Planck with either BAO + SN, ACT or SPT results in a marginal shift of the peaks of the posteriors toward a nonzero b. In the case of the BAO + SN, it is due to the mild preference of the BAO data, when analyzed in a recombination-model-independent way [114,115], for a smaller value of the sound horizon at decoupling, $r_{\rm drag}$, and, hence, a larger H_0, and the fact that clumping reduces $r_{\rm drag}$.

Adding SPT to the combination of Planck + BAO + SN further increases the peak values of b and H_0, while adding ACT has the opposite effect, in line with our earlier results. Adding ACT data results in a notable tightening of the clumping posterior, lowering the upper bound on b. The 95% c.l. upper bounds on clumping from Planck + SPT + BAO + SN and Planck + ACT + BAO + SN are $b < 0.50$ and $b < 0.34$, respectively, with additional parameter constraints provided in Table IV in the Appendix. For completeness, the mean parameter values and the 68% c.l. uncertainties in the ΛCDM model for the same data combinations are also provided in the Appendix (Table III).

The right panel of Fig. 11 shows the impact of adding the SH0ES prior (H0) to the datasets shown in the left panel. Fitting the ΛCDM + b model to Planck + H0 gives $b = 0.48 \pm 0.19$ and $H_0 = 70.32 \pm 0.85$ km/s/Mpc. Adding the BAO and SN data results in $b = 0.40^{+0.15}_{-0.19}$ and $H_0 = 69.68 \pm 0.67$ km/s/Mpc, a reduction that is generally expected for all models that aim to relieve the Hubble tension by reducing the sound horizon [85]. Further combing Planck + BAO + SN + H0 with the SPT data slightly increases the mean values, giving $b = 0.41^{+0.14}_{-0.18}$ and $H_0 = 69.70 \pm 0.63$ km/s/Mpc. On the other hand, adding ACT to Planck + BAO + SN + H0 brings the clumping down to $b = 0.27^{+0.11}_{-0.15}$, with $H_0 = 69.15 \pm 0.56$ km/s/Mpc. The global fit to Planck + ACT + STP + BAO + SN + H0 gives $b = 0.31^{+0.11}_{-0.15}$ and $H_0 = 69.28 \pm 0.56$ km/s/Mpc, while reducing the total χ^2 by 5.5 compared to the ΛCDM fit to the same data combination. Additional parameter constraints obtained with the SH0ES prior are presented in Table V in the Appendix. The prior shifts the constraints along the degeneracy axis in the b-H_0 plane. This results in a clear preference for a nonzero b for all data combinations, though the significance of the clumping detection is reduced from $\sim 3\sigma$ to $\sim 2\sigma$ when ACT data is included.

Table VI (see the Appendix) summarizes the best-fit χ^2 values for the individual datasets in the LCDM and ΛCDM + b models. When comparing the ΛCDM fits to those of ΛCDM + b for the same data combinations, with and without the SH0ES prior, we see that the χ^2 of Planck (plik), BAO and SN do not change significantly with a nonzero clumping and a higher H_0, while the SPT-3G χ^2 is reduced and the ACT χ^2 is increased. This is consistent with the mild tension between SPT-3G and ACT discussed extensively in Sec. III.

We note that, in addition to helping to relieve the Hubble tension, the ΛCDM + b model also improves the

[10] The BAO data-analysis pipelines include the use of ΛCDM templates which might introduce a bias when analysing the ΛCDM + b model. However, preliminary studies from [96] suggest that the impact of b on the BAO templates might be small enough to be ignored.

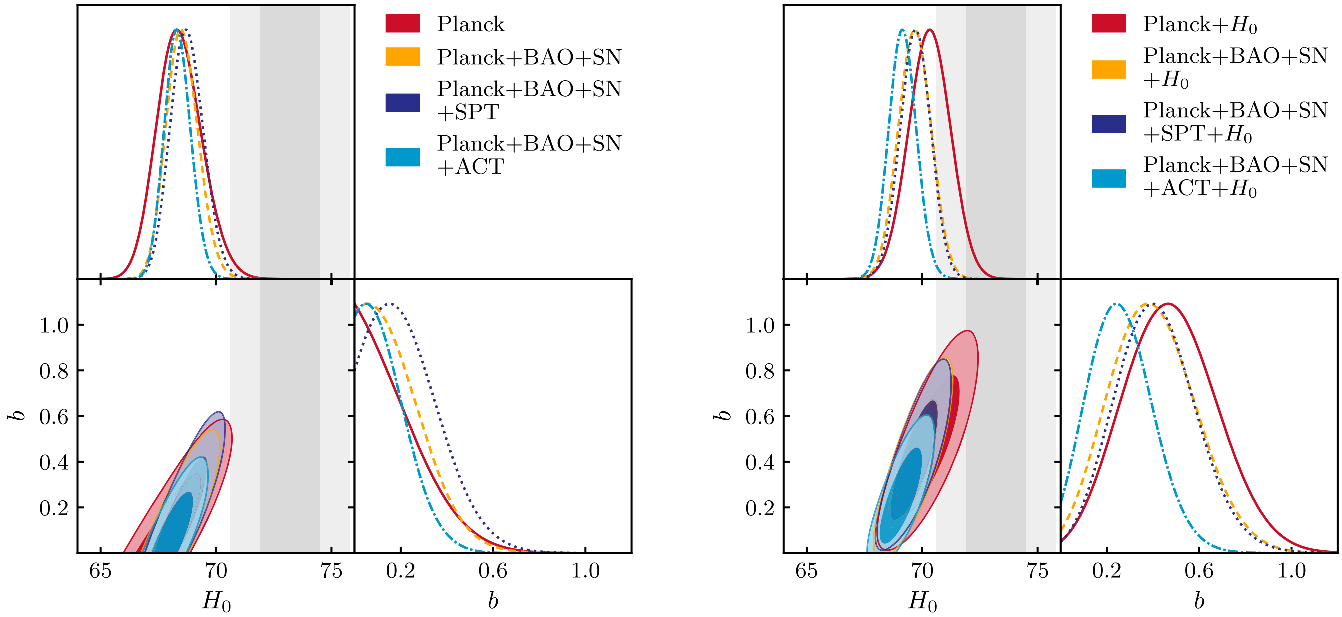

FIG. 11. *Left panel:* Constraints on the clumping factor b and H_0 from Planck only (red), the combination of Planck with BAO and SN data (orange), and with SPT-3G 2018 (dark blue) and ACT DR4 (light blue). The vertical gray band indicates the 2σ range of the latest H_0 measurement by the SH0ES team [70]. Adding the SPT-3G 2018 data to Planck + BAO + SN relaxes the 95% c.l. bound on b from 0.43 to 0.50, while adding the ACT DR4 data tightens it to $b < 0.34$. *Right panel:* Same as the left panel, but now including the SH0ES result as a prior on H_0. With the H_0 prior, all data combinations show a clear preference for clumping, but the detection significance is reduced from $\sim 3\sigma$ to $\sim 2\sigma$ when the ACT DR4 data is included.

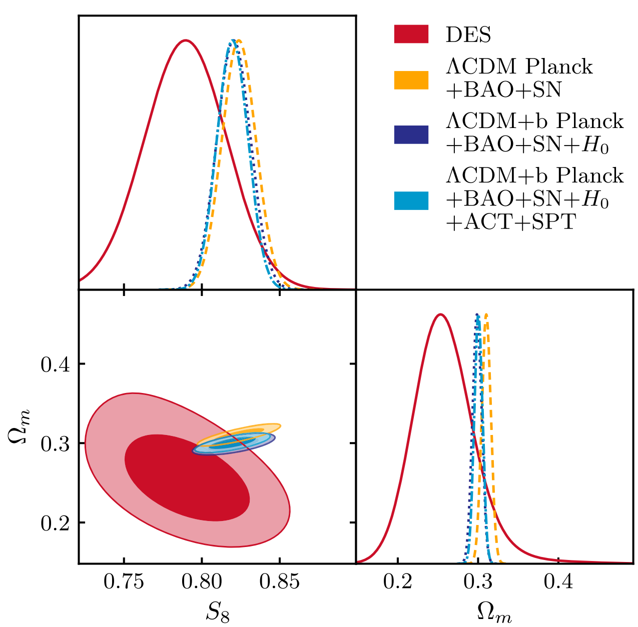

FIG. 12. Joint constraints in the S_8-Ω_m plane from Planck + BAO + SN in ΛCDM (orange), in ΛCDM + b with a SH0ES-based H_0 prior (dark blue), and when adding SPT-3G 2018 and ACT DR4 data to the latter (light blue). We also show the ΛCDM based constraints from the DES Y1 data [116] in red. There is a slight relief of the tension in ΛCDM + b due to $\Omega_m h^2$ remaining largely the same as in the best-fit ΛCDM model, while h is increased.

agreement between the matter clustering amplitude (quantified by the S_8-Ω_m values) in the Planck best-fit ΛCDM model and that obtained by the galaxy weak lensing surveys such as DES [88,116] and KiDS [87,117]. Figure 12 compares the S_8-Ω_m joint posteriors in the Planck + BAO + SN best-fit ΛCDM model to those in ΛCDM + b with and without the ACT and SPT data, together with the DES Y1 contours.[11] The primary reason for the lower S_8 and Ω_m values in the clumping mode is the fact that $\Omega_m h^2$ remains largely the same as in ΛCDM, while h is increased.

Summarizing the current status of the ΛCDM + b model, it is clear that it is limited in its ability to fully resolve the Hubble tension, only allowing values of $H_0 \lesssim 70$ km/s/Mpc. However, even if the H_0 tension was not fully relieved in this model, a clear detection of clumping is interesting by itself as it would be a tantalizing (albeit indirect) evidence of the PMF. Alternatively, a nondetection of clumping would provide the tightest constraint on the PMF strength.

V. FORECASTS

In this section, we forecast the constraints on the ΛCDM + b model for ongoing and future experiments.

[11] The DES Y3 data [88] are in slightly better agreement with Planck due to a higher Ω_m. However the DES-Y3 likelihood was not yet available at the time of completion of this paper.

We consider three experimental configurations: the full SPT-3G survey [90], SO [118] and CMB-S4, a next-generation ground-based CMB experiment [119]. In all three cases, we consider the combination of the lensed TT,TE,EE power spectra, while setting a Gaussian prior on the optical depth to reionization of $\sigma(\tau) = 0.007$, and do not include the reconstructed CMB lensing spectra. We assume the ΛCDM Planck best-fit, with $b = 0$, as our fiducial model.

A. Experiments

SPT-3G. The constraints showed in the previous sections are derived from the SPT-3G TE,EE spectra observed in 2018. This data was collected from only half of a typical observing season, during which half of the detectors were operable. For the forecast presented in this section, we consider five observation seasons (2019–2023 included), which will use all ∼16,000 detectors on the main survey field (∼1500 deg^2, $f_{sky} \sim 0.03$). We include three frequency bands, 95, 150, and 220 GHz, in both intensity and polarization, with beam full-width half-maximum (FWHM) of 1.7, 1.2, and 1.1 arcminutes (arcmin), respectively, and projected white noise levels in temperature of 3.0, 2.2, and 8.8 μK-arcmin (a factor of $\sqrt{2}$ higher in polarization) [90,120]. The noise curves also include the atmospheric $1/f$ noise and account for foreground residuals. The multipole range considered is $\ell = 100$–5000.

SO is a CMB experiment being built in the Atacama desert in Chile. We use the noise curves for the large-aperture (LAT) 6-m telescope described in [118], which will observe 40% of the sky ($f_{sky} \sim 0.4$) in six frequency bands at 27, 39, 93, 145, 225 and 280 GHz. We consider both the baseline and goal sensitivity levels, which correspond to white noise levels in intensity of 8, 10, and 22 μK-arcmin or 5.8, 6.3, 15 μK-arcmin at the CMB frequencies of 93, 145 and 225 GHz (a factor of $\sqrt{2}$ higher in polarization), with the beam FWHM of 2.2, 1.4, and 1.0 arcmin, respectively. The noise curves include contributions from the atmospheric $1/f$ noise and foreground uncertainties from component separation (we use the "Deproj-0" configuration from [121], described in [118]), but also make use of Planck data at large angular scales. The multipole range considered is $\ell = 40$–5000.

CMB-S4 is a next-generation ground-based CMB experiment. It will be located in the Atacama desert in Chile and at the South Pole [119], for a wide and a deep area survey, respectively. It will cover frequencies from 20 to 270 GHz. At the main CMB frequencies 93, 145 and 225 GHz, it will feature white noise levels in intensity of 1.5, 1.5, 4.8 μK-arcmin, with beam FWHMs of 2.2, 1.4, 1.0 arcmin respectively. We forecast the constraints of the wide survey from Chile, using the noise curves from [122], which combine information from all frequencies using an internal linear combination method. Similarly to the SO forecasts, that include the 1/f atmospheric noise and residual uncertainties from component separation. We assume $f_{sky} = 0.42$, which excludes the area covering the galaxy in the wide survey.

For joint constraints with Planck we regard the SPT data as independent. Due to the small survey footprint of the ground-based survey, we expect correlations to be negligible. When combining Planck with SO or CMB-S4 data, we consider Planck data in intensity and polarization at $\ell = 30$–2500 covering only the 30% of the sky which will not be observed by the ground based experiments. Additionally, we use the full Planck data in TT at $\ell < 30$, while we do not include polarization at large scales assuming that the information is already contained in the prior we set on τ.

B. Results

Figure 13 shows the results of the forecasts ("FC" in the figures) for SPT-3G, SO (which includes some Planck data at large multipoles) and CMB-S4. For SPT-3G, we also show the case where we combine with Planck data. We verified that for SO and CMB-S4 adding Planck data does not change the constraints. We forecast that the full SPT-3G survey will improve the upper limit on b by 50% compared to Planck, and, in combination with it, by more than a factor of 2.7. The future generation of CMB experiments will improve the Planck limits by a factor of 5.9 for SO goal (we find no appreciable difference using SO baseline) and 7.8

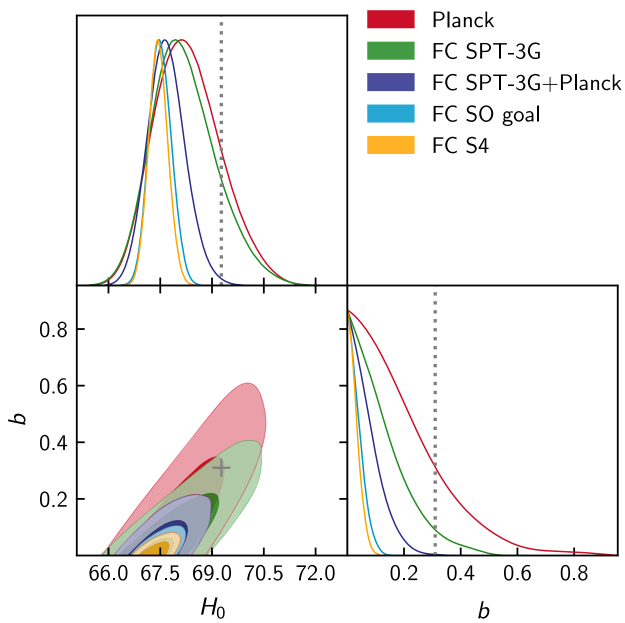

FIG. 13. Forecasts for b and H_0 for the full SPT-3G survey (green) and its combination with Planck (blue), for SO (light blue) and CMB-S4 (yellow), assuming a ΛCDM model as a fiducial. We show the real Planck results (red) as a reference. Future CMB experiments alone will be able to rule out the best-fit of Planck + ACT + SPT + BAO + SN + SH0ES in the ΛCDM + b model (gray dotted lines and the cross), i.e., representing the current ability of the clumping model to relieve the Hubble tension. Conversely, they will be able to detect such a clumping amplitude with some level of confidence.

for CMB-S4. We report full results for $\Lambda\mathrm{CDM} + b$ and $\Lambda\mathrm{CDM}$ in Tables VII and VIII in the Appendix, respectively. We note that, while for SPT-3G the constraints on H_0 will still weaken by about a factor of 2 in the $\Lambda\mathrm{CDM} + b$ model with respect to $\Lambda\mathrm{CDM}$, the sensitivity of CMB-S4 will break degeneracies sufficiently, so that constraints on H_0 and other parameters degrade by $< 10\%$ when adding baryon-clumping to $\Lambda\mathrm{CDM}$. In other words, future experiments, such as SO or CMB-S4, will have enough constraining power by themselves to either detect or rule out the values of clumping currently required to alleviate the Hubble tension. Taking the Planck + ACT + SPT + BAO + SN + SH0ES best-fit value of clumping presented in Sec. IV, $b = 0.31$ (also shown as a gray cross in Fig. 13), Planck+SPT-3G, SO and CMB-S4 will be able to either detect or rule out this value at the 3.5, 7.5, 9.7σ level, respectively. We note that a clumping value of $b = 0.31$ approximately corresponds to a pre-recombination comoving field strength of $B \approx 0.09$ nG [64].[12] The most stringent limit on clumping, forecasted for the CMB-S4 experiment, could constrain the pre-recombination PMF field strength to $B < 0.04$ nG at the 95% c.l.[13]

VI. CONCLUSIONS

Primordial magnetic fields, generated early in the history of the Universe, have long been considered as a way of explaining the observed galactic, cluster and intergalactic fields. The evidence for them has grown in recent years, with the blazar observations [123–125] and the discovery of magnetized filaments of cosmological extent [126]. While there is no firm theoretical prediction for the expected field strength, a pre-recombination PMF of ~0.05 nG comoving strength would simultaneously explain all observed magnetic fields. It is, therefore, quite intriguing that a PMF of the same strength could also help to relieve the Hubble tension. Indeed, the latter points at a missing ingredient in the physics of the Universe at the time of recombination, and many extensions of $\Lambda\mathrm{CDM}$ were proposed to help resolve the tension (see e.g., [127]). The baryon clumping induced by the PMF could be that ingredient, with no need to alter $\Lambda\mathrm{CDM}$.

With no new physics to invent, the PMF sourced clumping is a highly falsifiable proposal. Future CMB experiments, probing temperature and polarization anisotropies at higher resolution, will be able to conclusively confirm or rule it out. There is still uncertainty about the shape and evolution of the baryon PDF. Obtaining it would require numerical simulations of compressible MHD, which is a challenging, but not impossible, task. Hence, one can fully expect the baryon PDF to be known in due course. Until then, we used a simple model (M1) of clumping, introduced in [52], to derive the constraints on the clumping parameter b from the current data, including the recently published CMB data by ACT DR4 and SPT-3G 2018. We found that the two are in mild tension when it comes to b, with ACT tightening the Planck bound, and SPT weakly preferring nonzero clumping.

We have investigated potential sources of the difference in constraints. For the ACT data, they appear in part related to the amplitude of the TE spectrum, which has also been shown to cause tension with Planck data within the $\Lambda\mathrm{CDM}$ model. Overall, we find that ACT and Planck are in 2.4σ tension in $\Lambda\mathrm{CDM} + b$ compared to 2.7σ in $\Lambda\mathrm{CDM}$, while SPT and ACT are in 2.6 and 2.7σ tension in $\Lambda\mathrm{CDM}$ and $\Lambda\mathrm{CDM} + b$, respectively.

Our forecast shows that future high resolution CMB temperature measurements, such as the full-survey SPT-3G data, Simons Observatory, and CMB-S4, will provide a stringent test of this scenario, with the latter capable of constraining b down to 0.065 at 95% c.l. This corresponds to a pre-recombination PMF strength of ~0.04 nG, which would be the tightest constraint on a PMF.

Baryon clumping, like any other model that aims to reduce the Hubble tension by lowering the sound speed at recombination, can only raise the value of H_0 up to ~70 km/s/Mpc, which is still ~2σ lower than the SH0ES measurement. The distance ladder measurements of the Hubble constant may still change. However, even if baryon clumping did not fully resolve the Hubble tension, a conclusive detection of evidence for a PMF would be a major discovery in its own right, opening a new observational window into the processes that happened in the very early Universe.

ACKNOWLEDGMENTS

We are grateful to Karim Benabed, Bradford Benson, Thomas Crawford, Lloyd Knox and the SPT collaboration for insightful discussions and suggestions, and Srinivasan Raghunathan, Marco Raveri, Gong-Bo Zhao for their assistance. We thank Yacine Ali-Haïmoud, Julian Muñoz, Michael Rashkovetskyi and Leander Thiele for commenting on the manuscript. We gratefully acknowledge using GetDist [128]. This project has received funding from the European Research Council (ERC) under the European Union's Horizon 2020 research and innovation programme (Grant Agreement No. 101001897). This research was enabled in part by support provided by WestGrid [129] and Compute Canada Calcul Canada [130]. This research used resources of the IN2P3 Computer Center [131]. L. P. is supported in part by the National Sciences and Engineering

[12] It is important to note that the limits given in [64] are on post-recombination magnetic field strength. The relation between pre- and post-recombination field strength is dependent on the spectral index. Namely, $B_{\mathrm{post}} \approx B_{\mathrm{pre}}/6$ for phase transition produced fields, while $B_{\mathrm{post}} \approx B_{\mathrm{pre}}$ for inflationary produced scale-invariant fields. Moreover, due to the use of older 2013 data, the stated limits in [64] are a factor ~2 stronger than those from the most recent CMB data.

[13] The improvement in the constraint on the magnetic field strength B is not as drastic as that on the clumping factor b, as the latter scales as a high power of B, i.e., $b \propto B^x$, with $x \approx 3$–4.

Research Council (NSERC) of Canada. L. B. acknowledges support from the University of Melbourne and the Australian Research Council (DP210102386).

APPENDIX: ADDITIONAL TABLES

We present our full results in the following tables. We report the constraints on cosmological parameters from the Planck + BAO + SN data with the addition of SPT-3G 2018 and ACT DR4. In Table III we show results for the ΛCDM model, whereas we focus on ΛCDM + b in Tables IV and V without and with a SH0ES-based prior on H_0, respectively. Table VI shows the best-fit χ^2 values for the models and data combinations considered in Sec. IV. Finally, we present forecast parameter constraints for the ΛCDM + b and ΛCDM model in Tables VIII and VIII, respectively.

TABLE III. Mean parameter values and 68% c.l. uncertainties in ΛCDM for Planck + BAO + SN and with the addition of the SPT-3G 2018 and ACT DR4 datasets.

	ΛCDM Planck + BAO + SN			
		+SPT-3G 2018	+ACT DR4	+SPT-3G 2018 +ACT DR4
$\Omega_b h^2$	$0.02243 + 0.00013$	$0.02245 + 0.00012$	$0.02240 + 0.00012$	$0.02242 + 0.00011$
$\Omega_c h^2$	$0.11920 + 0.00090$	$0.11893 + 0.00086$	$0.11920 + 0.00085$	$0.11898 + 0.00085$
$100\theta_{MC}$	$1.04101 + 0.00029$	$1.04079 + 0.00027$	$1.04115 + 0.00027$	$1.04094 + 0.00025$
τ	$0.0565 + 0.0071$	$0.0563 + 0.0070$	$0.0554 + 0.0070$	$0.0553 + 0.0069$
$\ln(10^{10}A_s)$	$3.047 + 0.014$	$3.045 + 0.014$	$3.052 + 0.014$	$3.050 + 0.013$
n_s	$0.9671 + 0.0036$	$0.9679 + 0.0036$	$0.9693 + 0.0034$	$0.9699 + 0.0033$
H_0	$67.72 + 0.40$	$67.76 + 0.38$	$67.74 + 0.38$	$67.77 + 0.37$
Ω_m	$0.3103 + 0.0054$	$0.3094 + 0.0051$	$0.3100 + 0.0051$	$0.3093 + 0.0050$
σ_8	$0.8101 + 0.0059$	$0.8084 + 0.0057$	$0.8132 + 0.0057$	$0.8113 + 0.0055$
S_8	$0.824 + 0.010$	$0.8209 + 0.0096$	$0.8267 + 0.0099$	$0.8238 + 0.0095$
$r_\star$	$144.59 + 0.21$	$144.65 + 0.21$	$144.62 + 0.21$	$144.66 + 0.21$

TABLE IV. Mean parameter values and along with the 68% c.l. uncertainties in the ΛCDM + b model for Planck + BAO + SN and with the addition of the SPT-3G 2018 and ACT DR4 datasets. The 95% c.l. limits on the clumping factor b are given in parentheses.

	ΛCDM + b Planck + BAO + SN			
		+SPT-3G 2018	+ACT DR4	+SPT-3G 2018 +ACT DR4
b	$<0.231(0.434)$	$0.232^{+0.087}_{-0.19}(0.497)$	$0.145^{+0.033}_{-0.14}(0.336)$	$0.175^{+0.063}_{-0.15}(0.378)$
$\Omega_b h^2$	0.02242 ± 0.00014	0.02244 ± 0.00012	0.02236 ± 0.00012	0.02237 ± 0.00011
$\Omega_c h^2$	$0.1209^{+0.0013}_{-0.0015}$	$0.1210^{+0.0013}_{-0.0015}$	$0.1206^{+0.0011}_{-0.0013}$	$0.1206^{+0.0012}_{-0.0014}$
$100\theta_{MC}$	$1.0452^{+0.0018}_{-0.0034}$	$1.0459^{+0.0024}_{-0.0033}$	$1.0445^{+0.0014}_{-0.0027}$	$1.0449^{+0.0018}_{-0.0028}$
τ	0.0535 ± 0.0072	0.0523 ± 0.0072	0.0526 ± 0.0071	0.0518 ± 0.0073
$\ln(10^{10}A_s)$	3.042 ± 0.014	3.038 ± 0.014	3.046 ± 0.014	3.042 ± 0.014
n_s	0.9618 ± 0.0045	0.9619 ± 0.0044	0.9644 ± 0.0043	0.9644 ± 0.0043
H_0	$68.54^{+0.56}_{-0.73}$	$68.74^{+0.61}_{-0.74}$	$68.34^{+0.48}_{-0.59}$	$68.48^{+0.52}_{-0.59}$
Ω_m	0.3065 ± 0.0058	0.3049 ± 0.0056	0.3076 ± 0.0053	0.3063 ± 0.0053
σ_8	0.8162 ± 0.0071	$0.8157^{+0.0068}_{-0.0077}$	0.8174 ± 0.0063	0.8163 ± 0.0064
S_8	0.825 ± 0.010	0.8223 ± 0.0098	0.8277 ± 0.0097	0.8249 ± 0.0096
$r_\star$	$143.58^{+0.80}_{-0.51}$	$143.42^{+0.82}_{-0.62}$	$143.81^{+0.66}_{-0.42}$	$143.71^{+0.69}_{-0.50}$

TABLE V. Mean parameter values and 68% c.l. uncertainties in ΛCDM + b for Planck + BAO + SN with a SH0ES-based prior on H_0 and the SPT-3G 2018 and ACT DR4 datasets.

	ΛCDM + b Planck + BAO + SN + H_0			
		+SPT-3G 2018	+ACT DR4	+SPT-3G 2018 +ACT DR4
b	$0.40^{+0.15}_{-0.19}$	$0.41^{+0.14}_{-0.18}$	$0.27^{+0.11}_{-0.15}$	$0.31^{+0.11}_{-0.15}$
$\Omega_b h^2$	0.02253 ± 0.00014	0.02252 ± 0.00012	0.02242 ± 0.00012	0.02242 ± 0.00011
$\Omega_c h^2$	0.1218 ± 0.0015	0.1217 ± 0.0014	0.1209 ± 0.0014	0.1211 ± 0.0014
$100\theta_{MC}$	1.0493 ± 0.0028	$1.0493^{+0.0027}_{-0.0025}$	1.0471 ± 0.0024	1.0476 ± 0.0024
τ	0.0531 ± 0.0074	0.0517 ± 0.0072	0.0528 ± 0.0072	0.0515 ± 0.0072
$\ln(10^{10} A_s)$	3.041 ± 0.014	3.037 ± 0.014	3.045 ± 0.014	3.041 ± 0.014
n_s	$0.9603^{+0.0038}_{-0.0043}$	0.9608 ± 0.0039	$0.9632^{+0.0040}_{-0.0045}$	$0.9631^{+0.0038}_{-0.0043}$
H_0	69.68 ± 0.67	69.70 ± 0.63	69.15 ± 0.56	69.28 ± 0.56
Ω_m	0.2987 ± 0.0053	0.2982 ± 0.0051	0.3011 ± 0.0050	0.3004 ± 0.0048
σ_8	0.8223 ± 0.0080	0.8205 ± 0.0075	0.8199 ± 0.0068	0.8192 ± 0.0068
S_8	0.820 ± 0.010	0.8179 ± 0.0097	0.8214 ± 0.0098	0.8197 ± 0.0094
$r_\star$	142.71 ± 0.75	142.73 ± 0.70	143.35 ± 0.63	143.20 ± 0.64

TABLE VI. The best-fit χ^2 values for the models and data combinations considered in Sec. IV. The SPT-3G 2018 and ACT DR4 datasets are abbreviated as *SPT* and *ACT*, respectively.

	ΛCDM Planck + BAO + SN				ΛCDM + b Planck + BAO + SN				ΛCDM + b Planck + BAO + SN + H_0			
		+SPT	+ACT	+SPT + ACT		+SPT	+ACT	+SPT + ACT		+SPT	+ACT	+SPT + ACT
$\chi^2_{\rm plik}$	2346.71	2348.71	2349.4	2350.29	2346.72	2350.45	2347.6	2351.83	2350.98	2352.2	2348.35	2349.48
$\chi^2_{\rm lowl}$	23.60	23.37	22.28	22.32	24.14	24.10	23.55	22.87	23.98	24.96	22.87	23.23
$\chi^2_{\rm simall}$	396.71	397.27	397.95	396.05	395.8	396.62	395.79	395.84	395.68	397.55	395.73	395.78
$\chi^2_{\rm lensing}$	8.63	8.57	8.87	8.85	9.18	8.68	8.86	8.84	8.93	8.74	8.86	9.04
$\chi^2_{\rm BAO}$	17.58	17.27	17.10	17.47	17.13	17.05	17.31	17.20	17.81	18.15	17.03	17.86
$\chi^2_{\rm SN}$	1035.08	1035.0	1034.93	1035.06	1034.96	1034.92	1035.01	1034.76	1034.73	1034.75	1034.78	1034.74
$\chi^2_{\rm SPT}$	…	1125.76	…	1130.01	…	1127.94	…	1130.07	…	1124.09	…	1126.92
$\chi^2_{\rm ACT}$	…	…	237.56	238.67	…	…	241.23	238.59	…	…	240.94	242.89

TABLE VII. Forecasts of constraints on cosmological parameters in the ΛCDM + b model for the full SPT-3G 5-year survey (*SPT-3G Y5*) by itself and jointly with Planck, SO and CMB-S4. We also show the error bars from the real Planck data for comparison. For each future experiment, the first column shows the 1σ error bars (or the 95% c.l. upper limit for b), while the second shows the improvement with respect to Planck as the ratio of the uncertainties. Note that the forecasts do not include CMB lensing, which is expected to further contribute to the tightening of the constraints.

	Planck	SPT-3G Y5		SPT-3G Y5 + Planck		SO goal		CMB-S4	
	σ_p	σ	σ_p/σ	σ	σ_p/σ	σ	σ_p/σ	σ	σ_p/σ
b	<0.5	<0.33	1.5	<0.18	2.7	<0.085	5.9	<0.065	7.8
H_0	0.93	0.98	0.95	0.56	1.7	0.32	2.9	0.28	3.3
$\Omega_{\rm b} h^2$	0.00015	0.00015	1	$9.3e$–05	1.6	$5.4e$–05	2.9	$3.8e$–05	4
$\Omega_{\rm c} h^2$	0.0014	0.0017	0.83	0.0012	1.2	0.00072	2	0.00064	2.2
τ	0.0073	0.0068	1.1	0.0064	1.2	0.0055	1.3	0.0051	1.4
$n_{\rm s}$	0.0046	0.0079	0.58	0.0038	1.2	0.0027	1.7	0.0025	1.9
$\ln(10^{10} A_{\rm s})$	0.014	0.013	1.1	0.012	1.2	0.0097	1.5	0.0088	1.6
$\Omega_{\rm m}$	0.0087	0.012	0.75	0.007	1.2	0.0043	2	0.0038	2.3
S_8	0.013	0.02	0.66	0.013	1	0.006	2.1	0.0048	2.7
σ_8	0.0072	0.0068	1.1	0.0056	1.3	0.003	2.4	0.0025	2.9
r_*	0.7	0.53	1.3	0.37	1.9	0.21	3.3	0.18	3.8

TABLE VIII. Forecasts of constraints on cosmological parameters as in Table VII, but for the ΛCDM model.

	Planck	SPT-3G Y5		SPT-3G Y5 + Planck		SO goal		CMB-S4	
	σ_p	σ	σ_p/σ	σ	σ_p/σ	σ	σ_p/σ	σ	σ_p/σ
H_0	0.54	0.66	0.81	0.47	1.2	0.28	1.9	0.25	2.2
$\Omega_b h^2$	0.00015	0.00014	1	$8.9e$–05	1.6	$4.9e$–05	3	$3.7e$–05	4
$\Omega_c h^2$	0.0012	0.0017	0.69	0.0012	1	0.00072	1.6	0.00065	1.8
τ	0.0075	0.0068	1.1	0.0064	1.2	0.0055	1.4	0.0052	1.5
n_s	0.0041	0.0076	0.54	0.0033	1.2	0.0024	1.7	0.0022	1.8
$\ln(10^{10}A_s)$	0.015	0.013	1.1	0.012	1.2	0.0096	1.5	0.0089	1.6
Ω_m	0.0073	0.0099	0.74	0.0068	1.1	0.0042	1.7	0.0037	2
S_8	0.013	0.018	0.7	0.013	1	0.0058	2.2	0.0044	2.9
σ_8	0.006	0.0067	0.9	0.0055	1.1	0.003	2	0.0025	2.4
r_*	0.26	0.44	0.6	0.28	0.94	0.18	1.5	0.17	1.6

[1] R. Durrer and A. Neronov, Astron. Astrophys. Rev. **21**, 62 (2013).
[2] K. Subramanian, Rep. Prog. Phys. **79**, 076901 (2016).
[3] T. Vachaspati, Rep. Prog. Phys. **84**, 074901 (2021).
[4] T. Vachaspati, Phys. Lett. B **265**, 258 (1991).
[5] M. S. Turner and L. M. Widrow, Phys. Rev. D **37**, 2743 (1988).
[6] B. Ratra, Astrophys. J. **391**, L1 (1992).
[7] R. Crittenden, R. L. Davis, and P. J. Steinhardt, Astrophys. J. **417**, L13 (1993).
[8] A. Kosowsky and A. Loeb, Astrophys. J. **469**, 1 (1996).
[9] K. Jedamzik, V. Katalinic, and A. V. Olinto, Phys. Rev. D **57**, 3264 (1998).
[10] K. Jedamzik, V. Katalinic, and A. V. Olinto, Phys. Rev. Lett. **85**, 700 (2000).
[11] K. Subramanian and J. D. Barrow, Phys. Rev. D **58**, 083502 (1998).
[12] K. Subramanian and J. D. Barrow, Phys. Rev. Lett. **81**, 3575 (1998).
[13] R. Durrer, P. G. Ferreira, and T. Kahniashvili, Phys. Rev. D **61**, 043001 (2000).
[14] T. R. Seshadri and K. Subramanian, Phys. Rev. Lett. **87**, 101301 (2001).
[15] A. Mack, T. Kahniashvili, and A. Kosowsky, Phys. Rev. D **65**, 123004 (2002).
[16] K. Subramanian and J. D. Barrow, Mon. Not. R. Astron. Soc. **335**, L57 (2002).
[17] K. Subramanian, T. R. Seshadri, and J. Barrow, Mon. Not. R. Astron. Soc. **344**, L31 (2003).
[18] S. Mollerach, D. Harari, and S. Matarrese, Phys. Rev. D **69**, 063002 (2004).
[19] S. K. Sethi and K. Subramanian, Mon. Not. R. Astron. Soc. **356**, 778 (2005).
[20] A. Lewis, Phys. Rev. D **70**, 043518 (2004).
[21] G. Chen, P. Mukherjee, T. Kahniashvili, B. Ratra, and Y. Wang, Astrophys. J. **611**, 655 (2004).
[22] A. Lewis, Phys. Rev. D **70**, 043011 (2004).
[23] C. Scoccola, D. Harari, and S. Mollerach, Phys. Rev. D **70**, 063003 (2004).
[24] A. Kosowsky, T. Kahniashvili, G. Lavrelashvili, and B. Ratra, Phys. Rev. D **71**, 043006 (2005).
[25] H. Tashiro, N. Sugiyama, and R. Banerjee, Phys. Rev. D **73**, 023002 (2006).
[26] T. Kahniashvili and B. Ratra, Phys. Rev. D **71**, 103006 (2005).
[27] A. Zizzo and C. Burigana, New Astron. **11**, 1 (2005).
[28] I. Brown and R. Crittenden, Phys. Rev. D **72**, 063002 (2005).
[29] D. Yamazaki, K. Ichiki, T. Kajino, and G. J. Mathews, Astrophys. J. **646**, 719 (2006).
[30] M. Giovannini, Classical Quantum Gravity **23**, 4991 (2006).
[31] T. Kahniashvili and B. Ratra, Phys. Rev. D **75**, 023002 (2007).
[32] M. Giovannini and K. E. Kunze, Phys. Rev. D **77**, 063003 (2008).
[33] T. Seshadri and K. Subramanian, Phys. Rev. Lett. **103**, 081303 (2009).
[34] C. Caprini, F. Finelli, D. Paoletti, and A. Riotto, J. Cosmol. Astropart. Phys. 06 (2009) 021.
[35] D. G. Yamazaki, K. Ichiki, T. Kajino, and G. J. Mathews, Phys. Rev. D **81**, 023008 (2010).
[36] D. Paoletti and F. Finelli, Phys. Rev. D **83**, 123533 (2011).
[37] J. R. Shaw and A. Lewis, Phys. Rev. D **86**, 043510 (2012).
[38] K. E. Kunze, Phys. Rev. D **83**, 023006 (2011).
[39] R.-G. Cai, B. Hu, and H.-B. Zhang, J. Cosmol. Astropart. Phys. 08 (2010) 025.
[40] P. Trivedi, K. Subramanian, and T. R. Seshadri, Phys. Rev. D **82**, 123006 (2010).
[41] I. A. Brown, Astrophys. J. **733**, 83 (2011).

[42] M. Shiraishi, D. Nitta, S. Yokoyama, K. Ichiki, and K. Takahashi, Phys. Rev. D **82**, 121302 (2010); **83**, 029901(E) (2011).
[43] M. Shiraishi, D. Nitta, S. Yokoyama, K. Ichiki, and K. Takahashi, Phys. Rev. D **83**, 123003 (2011).
[44] P. Trivedi, T. R. Seshadri, and K. Subramanian, Phys. Rev. Lett. **108**, 231301 (2012).
[45] K. E. Kunze, Phys. Rev. D **85**, 083004 (2012).
[46] D. Paoletti and F. Finelli, Phys. Lett. B **726**, 45 (2013).
[47] A. Yadav, L. Pogosian, and T. Vachaspati, Phys. Rev. D **86**, 123009 (2012).
[48] L. Pogosian, T. Vachaspati, and A. Yadav, Can. J. Phys. **91**, 451 (2013).
[49] K. E. Kunze and E. Komatsu, J. Cosmol. Astropart. Phys. 01 (2014) 009.
[50] M. Shiraishi and T. Sekiguchi, Phys. Rev. D **90**, 103002 (2014).
[51] P. Trivedi, K. Subramanian, and T. R. Seshadri, Phys. Rev. D **89**, 043523 (2014).
[52] K. Jedamzik and T. Abel, J. Cosmol. Astropart. Phys. 10 (2013) 050.
[53] S. De, L. Pogosian, and T. Vachaspati, Phys. Rev. D **88**, 063527 (2013).
[54] J. Ganc and M. S. Sloth, J. Cosmol. Astropart. Phys. 08 (2014) 018.
[55] M. Ballardini, F. Finelli, and D. Paoletti, J. Cosmol. Astropart. Phys. 10 (2015) 031.
[56] K. E. Kunze and E. Komatsu, J. Cosmol. Astropart. Phys. 06 (2015) 027.
[57] T. Kahniashvili, Y. Maravin, G. Lavrelashvili, and A. Kosowsky, Phys. Rev. D **90**, 083004 (2014).
[58] P. A. R. Ade *et al.* (Planck Collaboration), Astron. Astrophys. **594**, A19 (2016).
[59] J. Chluba, D. Paoletti, F. Finelli, and J.-A. RubiÒo-Martín, Mon. Not. R. Astron. Soc. **451**, 2244 (2015).
[60] A. Zucca, Y. Li, and L. Pogosian, Phys. Rev. D **95**, 063506 (2017).
[61] D. R. Sutton, C. Feng, and C. L. Reichardt, Astrophys. J. **846**, 164 (2017).
[62] D. Paoletti, J. Chluba, F. Finelli, and J. A. Rubino-Martin, Mon. Not. R. Astron. Soc. **484**, 185 (2019).
[63] L. Pogosian and A. Zucca, Classical Quantum Gravity **35**, 124004 (2018).
[64] K. Jedamzik and A. Saveliev, Phys. Rev. Lett. **123**, 021301 (2019).
[65] N. Aghanim *et al.* (Planck Collaboration), Astron. Astrophys. **641**, A5 (2020).
[66] C. L. Bennett *et al.* (WMAP Collaboration), Astrophys. J. Suppl. Ser. **208**, 20 (2013).
[67] D. Dutcher *et al.* (SPT-3G Collaboration), Phys. Rev. D **104**, 022003 (2021).
[68] S. K. Choi *et al.* (ACT Collaboration), J. Cosmol. Astropart. Phys. 12 (2020) 045.
[69] K. Jedamzik and L. Pogosian, Phys. Rev. Lett. **125**, 181302 (2020).
[70] A. G. Riess, S. Casertano, W. Yuan, J. B. Bowers, L. Macri, J. C. Zinn, and D. Scolnic, Astrophys. J. Lett. **908**, L6 (2021).
[71] A. G. Riess, W. Yuan, L. M. Macri, D. Scolnic, D. Brout, S. Casertano, D. O. Jones *et al.*, arXiv:2112.04510.
[72] N. Aghanim *et al.* (Planck Collaboration), Astron. Astrophys. **641**, A6 (2020).
[73] D. Pesce *et al.*, Astrophys. J. **891**, L1 (2020).
[74] K. C. Wong *et al.*, Mon. Not. R. Astron. Soc. **498**, 1420 (2020).
[75] A. J. Shajib *et al.* (DES Collaboration), Mon. Not. R. Astron. Soc. **494**, 6072 (2020).
[76] D. Harvey, Mon. Not. R. Astron. Soc. **498**, 2871 (2020).
[77] M. Millon *et al.*, Astron. Astrophys. **639**, A101 (2020).
[78] W. L. Freedman, B. F. Madore, T. Hoyt, I. S. Jang, R. Beaton, M. G. Lee, A. Monson, J. Neeley, and J. Rich, Astrophys. J. **891**, 57 (2020).
[79] M. M. Ivanov, M. Simonović, and M. Zaldarriaga, J. Cosmol. Astropart. Phys. 05 (2020) 042.
[80] G. d'Amico, J. Gleyzes, N. Kokron, K. Markovic, L. Senatore, P. Zhang, F. Beutler, and H. Gil-Marín, J. Cosmol. Astropart. Phys. 05 (2020) 005.
[81] S. Aiola *et al.* (ACT Collaboration), J. Cosmol. Astropart. Phys. 12 (2020) 047.
[82] S. Alam *et al.* (eBOSS Collaboration), Phys. Rev. D **103**, 083533 (2021).
[83] L. Knox and M. Millea, Phys. Rev. D **101**, 043533 (2020).
[84] M. Zaldarriaga and D. D. Harari, Phys. Rev. D **52**, 3276 (1995).
[85] K. Jedamzik, L. Pogosian, and G.-B. Zhao, Commun. Phys. **4**, 123 (2021).
[86] F.-Y. Cyr-Racine, F. Ge, and L. Knox, arXiv:2107.13000.
[87] C. Heymans, T. Tröster *et al.*, Astron. Astrophys. **646**, A140 (2021).
[88] T. M. C. Abbott *et al.* (DES Collaboration), arXiv: 2105.13549.
[89] S. W. Henderson *et al.*, J. Low Temp. Phys. **184**, 772 (2016).
[90] B. Benson *et al.* (SPT-3G Collaboration), Proc. SPIE Int. Soc. Opt. Eng. **9153**, 91531P (2014).
[91] J. Aguirre *et al.* (Simons Observatory Collaboration), arXiv:1808.07445.
[92] K. Abazajian *et al.*, arXiv:1907.04473.
[93] L. Thiele, Y. Guan, J. C. Hill, A. Kosowsky, and D. N. Spergel, Phys. Rev. D **104**, 063535 (2021).
[94] N. Lee and Y. Ali-Haïmoud, Phys. Rev. D **104**, 103509 (2021).
[95] K. Jedamzik and G. M. Fuller, Astrophys. J. **452**, 33 (1995).
[96] M. Rashkovetskyi, J. B. Muñoz, D. J. Eisenstein, and C. Dvorkin, Phys. Rev. D **104**, 103517 (2021).
[97] D. Scolnic *et al.*, Astrophys. J. **859**, 101 (2018).
[98] A. Lewis and S. Bridle, Phys. Rev. D **66**, 103511 (2002).
[99] S. Seager, D. D. Sasselov, and D. Scott, Astrophys. J. **523**, L1 (1999).
[100] R. Banerjee and K. Jedamzik, Phys. Rev. D **70**, 123003 (2004).
[101] A. Lewis and A. Challinor, Phys. Rev. D **76**, 083005 (2007).
[102] L. Senatore, S. Tassev, and M. Zaldarriaga, J. Cosmol. Astropart. Phys. 08 (2009) 031.
[103] S. Das *et al.*, J. Cosmol. Astropart. Phys. 04 (2014) 014.
[104] L. Balkenhol *et al.*, Phys. Rev. D **104**, 083509 (2021).
[105] G. E. Addison, Y. Huang, D. J. Watts, C. L. Bennett, M. Halpern, G. Hinshaw, and J. L. Weiland, Astrophys. J. **818**, 132 (2016).

[106] N. Aghanim *et al.* (Planck Collaboration), Astron. Astrophys. **607**, A95 (2017).
[107] Y. Ali-Haïmoud and C. M. Hirata, Phys. Rev. D **83**, 043513 (2011).
[108] G.-B. Zhao *et al.*, Mon. Not. R. Astron. Soc. **504**, 33 (2021).
[109] Y. Wang *et al.*, Mon. Not. R. Astron. Soc. **498**, 3470 (2020).
[110] J. Hou *et al.*, Mon. Not. R. Astron. Soc. **500**, 1201 (2020).
[111] H. du Mas des Bourboux *et al.*, Astrophys. J. **901**, 153 (2020).
[112] F. Beutler, C. Blake, M. Colless, D. Jones, L. Staveley-Smith, L. Campbell, Q. Parker, W. Saunders, and F. Watson, Mon. Not. R. Astron. Soc. **416**, 3017 (2011).
[113] A. J. Ross, L. Samushia, C. Howlett, W. J. Percival, A. Burden, and M. Manera, Mon. Not. R. Astron. Soc. **449**, 835 (2015).
[114] L. Pogosian, G.-B. Zhao, and K. Jedamzik, Astrophys. J. Lett. **904**, L17 (2020).
[115] W. Lin, X. Chen, and K. J. Mack, Astrophys. J. **920**, 159 (2021).
[116] T. M. C. Abbott *et al.* (DES Collaboration), Phys. Rev. D **98**, 043526 (2018).
[117] S. Joudaki *et al.*, Astron. Astrophys. **638**, L1 (2020).
[118] P. Ade *et al.* (Simons Observatory Collaboration), J. Cosmol. Astropart. Phys. 02 (2019) 056.
[119] K. N. Abazajian *et al.* (CMB-S4 Collaboration), arXiv: 1610.02743.
[120] A. N. Bender *et al.*, Proc. SPIE Int. Soc. Opt. Eng. **10708**, 1070803 (2018).
[121] J. C. Hill (private communication).
[122] https://cmb-s4.org/wiki/index.php/Survey_Performance_Expectations.
[123] A. Neronov and I. Vovk, Science **328**, 73 (2010).
[124] F. Tavecchio, G. Ghisellini, L. Foschini, G. Bonnoli, G. Ghirlanda, and P. Coppi, Mon. Not. R. Astron. Soc. **406**, L70 (2010).
[125] A. Taylor, I. Vovk, and A. Neronov, Astron. Astrophys. **529**, A144 (2011).
[126] F. Govoni, E. Orr, A. Bonafede, M. Iacobelli, R. Paladino, F. Vazza, M. Murgia, V. Vacca, G. Giovannini, L. Feretti *et al.*, Science **364**, 981 (2019).
[127] N. Schöneberg, G. F. Abellán, A. Pérez Sánchez, S. J. Witte, c. V. Poulin, and J. Lesgourgues, arXiv:2107.10291.
[128] A. Lewis, arXiv:1910.13970.
[129] www.westgrid.ca.
[130] www.computecanada.ca.
[131] http://cc.in2p3.fr.